

Supplemental document for: Evolution dynamics of thin liquid structures investigated by phase-field model

Yanchen Wu, Fei Wang, Sai Zheng, Britta Nestler

In this supplemental document, we present some details for modeling the evolution dynamics of thin liquid structures to support the main text. In sections S. I we discuss the influence of Peclet number on the droplet contact line movements. In section S. II, we provide the thermodynamic consistency and the energy dissipation law of the coupled model. In section S. III, we give the information for the number of discretization points N versus Cn . In section S. IV, we validate the phase-field model with Cox's theory and conduct a sharp interface limit analysis based on the simulation results.

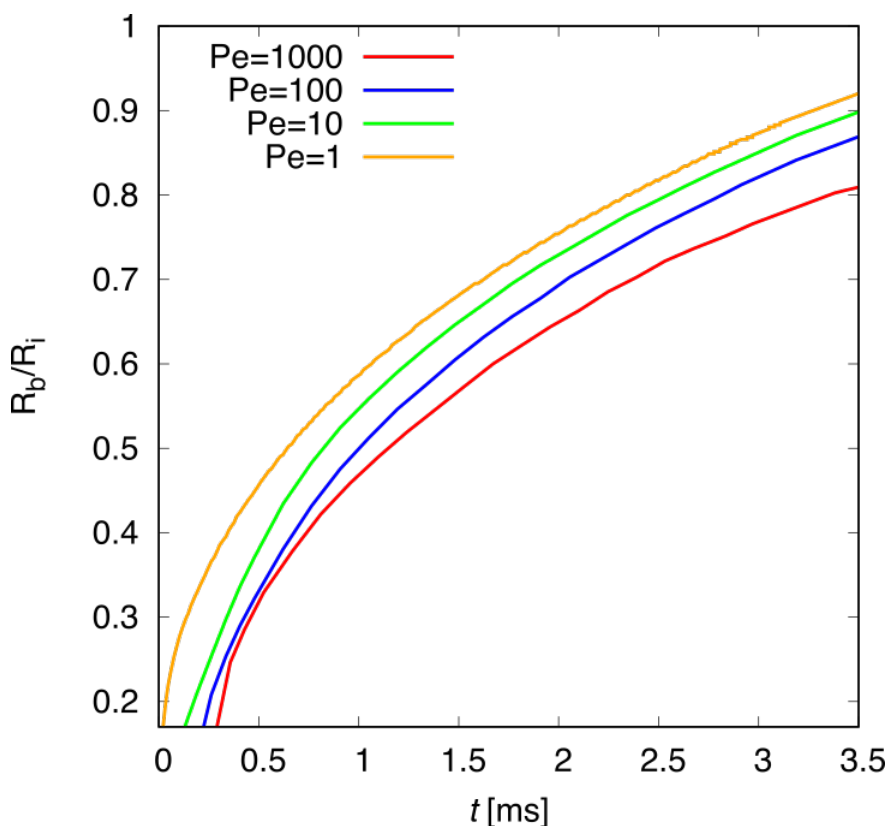


Figure S1: Time evolution of the base radius of a 2D-droplet spreading on a substrate with varying Pe . Here, the base radius R_b is rescaled by the initial radius $R_i = 0.82$ mm. We set $\tilde{\tau}_w = 1$ and $\theta_{eq} = 120^\circ$ for all of the four simulation cases.

S. I Discussion of Peclet number

The Peclet number (Pe) is a significant parameter in determining the interface motion and it is related to the diffusivity and interface mobility. As a phenomenological parameter in two-phase flows, the true value of Pe in the simulation is determined by comparing the simulation result with experimental data. Lower values of Pe significantly emphasize diffusion, slowing down the interface motion and making the model less representative of the real physical behavior. On the other hand, high values of Pe diminish the influence of diffusivity, possibly resulting in an unrealistic dominance of advection over diffusion. Fig. S1 shows the 2D simulation results for droplets spreading on a solid substrate with different values of Pe . It is found that as Pe decreases, the contact line motion slows down monotonously.

S. II Energy dissipation

Obeying the second law of thermodynamics, the total energy functional \mathcal{F}_{total} meets with

$$\frac{d\mathcal{F}_{total}}{dt} \leq 0, \quad (\text{S1})$$

where $\mathcal{F}_{total} = \mathcal{F} + \mathcal{F}_s + \mathcal{E}$ with \mathcal{E} denoting the kinetic energy of the whole system. \mathcal{F} dissipates as

$$\begin{aligned} \frac{d\mathcal{F}}{dt} &= \int_{\Omega} \left[\frac{df(c)}{dt} + 4\sigma\epsilon\nabla c \cdot \frac{d(\nabla c)}{dt} \right] d\Omega \\ &= \int_{\Omega} \left[\frac{\partial f(c)}{\partial c} \frac{dc}{dt} + 4\sigma\epsilon\nabla c \cdot \left(\nabla \frac{\partial c}{\partial t} + \mathbf{u} \cdot \nabla \nabla c \right) \right] d\Omega \\ &= \int_{\Omega} \left[\left(\frac{\partial f(c)}{\partial c} - 4\sigma\epsilon\nabla^2 c \right) \frac{dc}{dt} + 4\sigma\epsilon\nabla^2 c (\mathbf{u} \cdot \nabla c) + 4\sigma\epsilon\nabla c \cdot \mathbf{u} \cdot \nabla \nabla c \right] d\Omega \\ &= \int_{\Omega} \left[\Phi \frac{dc}{dt} + \nabla \cdot (4\sigma\epsilon\nabla c \otimes \nabla c) \cdot \mathbf{u} \right] d\Omega. \end{aligned} \quad (\text{S2})$$

The first term is related to the chemical potential and the second term is related to Kortweg stress tensor, which describes the transformation of the free energy into kinetic energy. \mathcal{F}_s dissipates as

$$\begin{aligned} \frac{d\mathcal{F}_s}{dt} &= \int_{\Omega} \left[4\sigma\epsilon\nabla c \cdot \frac{d(\nabla c)}{dt} \right] d\Omega + \int_S \frac{df_w(c)}{dt} dS \\ &= \int_{\Omega} \left[-4\sigma\epsilon\nabla^2 c \cdot \frac{dc}{dt} \right] d\Omega - \int_S (\gamma_{gs} - \gamma_s) l'(c) \frac{dc}{dt} dS \\ &= \int_S \left[4\sigma\epsilon\nabla c \cdot \mathbf{n} - (\gamma_{gs} - \gamma_s) l'(c) \right] \frac{dc}{dt} dS. \end{aligned} \quad (\text{S3})$$

Let the chemical potential at wall $\Phi_w = \frac{\delta \mathcal{F}_s}{\delta c} = 4\sigma\epsilon\nabla c \cdot \mathbf{n} - (\gamma_{gs} - \gamma_s)l'(c)$, the above equation becomes

$$\frac{d\mathcal{F}_s}{dt} = \int_S \Phi_w \frac{dc}{dt} dS. \quad (\text{S4})$$

According to the Navier-Stokes equations, the dissipation of the total kinetic energy is formulated as

$$\begin{aligned} \frac{d\mathcal{E}}{dt} &= \int_{\Omega} \rho \frac{d\mathbf{u}}{dt} \mathbf{u} d\Omega \\ &= \int_{\Omega} \nabla \cdot [(-p - \Phi c + f)\mathbf{I} - 4\sigma\epsilon\nabla \cdot (\nabla c \otimes \nabla c) + \mu(\nabla \mathbf{u} + \nabla \mathbf{u}^T)] \cdot \mathbf{u} d\Omega. \end{aligned} \quad (\text{S5})$$

We assume that the density does not change, and under the conditions of no-slip boundary condition and incompressible flow, we have

$$\int_{\Omega} [(-p - \Phi c + f)\mathbf{I}] \cdot \mathbf{u} d\Omega = 0. \quad (\text{S6})$$

Therefore, Eq. (S5) becomes

$$\frac{d\mathcal{E}}{dt} = \int_{\Omega} \nabla \cdot [-4\sigma\epsilon\nabla \cdot (\nabla c \otimes \nabla c) + \mu(\nabla \mathbf{u} + \nabla \mathbf{u}^T)] \cdot \mathbf{u} d\Omega. \quad (\text{S7})$$

The total free energy functional \mathcal{F}_{total} dissipates as

$$\frac{d\mathcal{F}_{total}}{dt} = \int_{\Omega} \Phi \frac{dc}{dt} + \nabla \cdot [\mu(\nabla \mathbf{u} + \nabla \mathbf{u}^T)] \cdot \mathbf{u} d\Omega + \int_S \Phi_w \frac{dc}{dt} dS. \quad (\text{S8})$$

From Eq. (3) and Eq. (21) in the main text, we know the time evolution of c , namely, dc/dt in the bulk domain and on the fluid-solid boundary S follows the Cahn-Hilliard and Allen-Cahn kinetics, respectively. Substituting dc/dt in Eq. (S8), we obtain

$$\begin{aligned} \frac{d\mathcal{F}_{total}}{dt} &= \int_{\Omega} \Phi \nabla \cdot (M \nabla \Phi) + \nabla \cdot [\mu(\nabla \mathbf{u} + \nabla \mathbf{u}^T)] \cdot \mathbf{u} d\Omega - \frac{1}{\tau_w} \int_S \Phi_w^2 dS \\ &= - \int_{\Omega} M (\nabla \Phi)^2 d\Omega - \int_{\Omega} \mu \nabla \mathbf{u} : \nabla \mathbf{u} d\Omega - \frac{1}{\tau_w} \int_S \Phi_w^2 dS \leq 0. \end{aligned} \quad (\text{S9})$$

The above derivation proves the thermodynamic consistency of the present CHNS model combined with Allen-Cahn type dynamic wetting boundary condition. As shown in the last term of Eq. (S9), the parameter τ_w controls the energy dissipation rate on the substrate.

S. III Number of discretization points N versus Cn

Table S1 lists the number of discretization points N versus Cn from simulation results.

Table S1: Number of discretization points N versus Cn .

Cn	1	2	4	6
N	2	4	8	12

S. IV Validation with Cox's theory and sharp interface limit analysis

In Figs. 3 and 4 of the main text, we compared the simulation results with experimental results in the literature. Here, we add an additional comparison of the simulation results of a droplet spreading on the substrate against the theoretical results of Cox^{1,2}. According to Cox's theory, the dynamic contact angle is determined by the viscous bending in the following manner:

$$g(\theta_D) = g(\theta_{eq}) + Ca \ln(\delta^{-1}). \quad (\text{S10})$$

The parameter δ is the ratio of the micrometer slip length (l_S) to a macroscopic length scale (e.g. droplet diameter). The capillary number $Ca = \mu U_w / \sigma$ with U_w denoting the

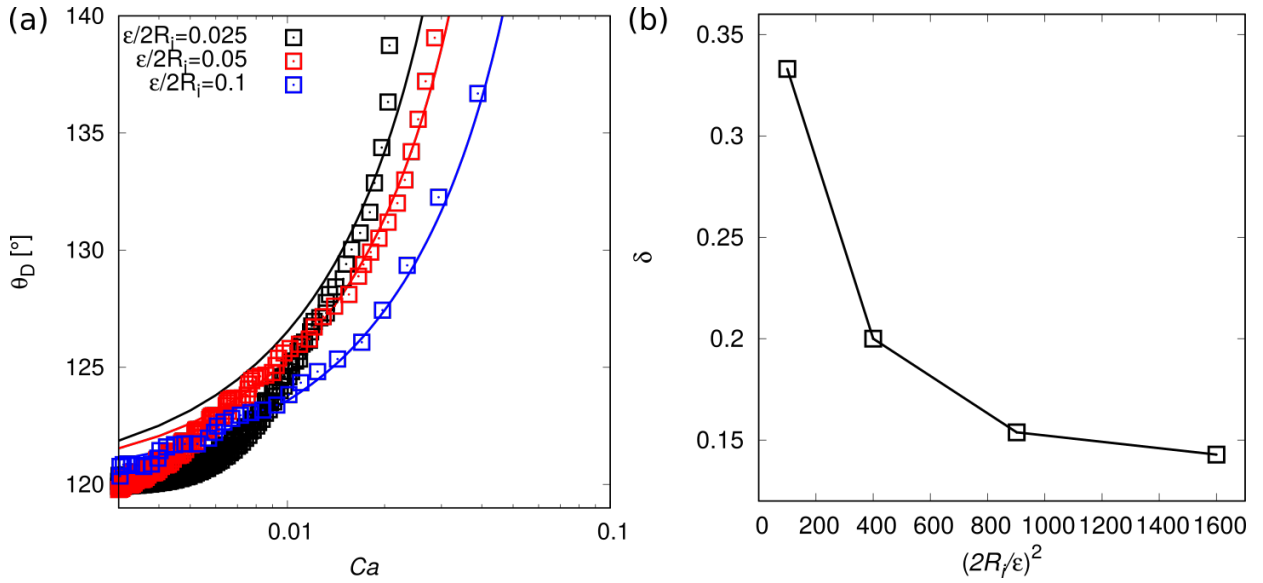


Figure S2: (a) Dynamic contact angle θ_D as a function of capillary number Ca when a droplet slowly spreads on a solid substrate with Young's contact angle $\theta_{eq} = 120^\circ$. The symbols with different colors indicate the results for droplets with different interface widths (initial radius R_i is constant) and the corresponding solid lines are Cox's theory $g(\theta_D) = g(\theta_{eq}) + Ca \ln(\delta^{-1})$ with different fitting parameters δ . The parameter δ is the ratio of the micrometer slip length to a macroscopic length scale (e.g. droplet diameter) (b) δ as a function of $(2R_i/\epsilon)^2$.

velocity of the contact line. The function $g(\theta)$ is given:

$$g(\theta) = \int_0^\theta \frac{\pi\alpha(\pi - \alpha) + (2\pi\alpha - \pi^2) \sin \alpha \cos \alpha - \pi \sin^2 \alpha}{2\pi^2 \sin \alpha} d\alpha. \quad (\text{S11})$$

Cox's theory is limited to small Ca and simple geometries. So we plot θ_D versus Ca in the range of $Ca < 0.1$. The different colored symbols indicate the simulation results for different values of $\varepsilon/2R_i$, where we reduce the interface width ($Cn = \text{const.}$, but mesh resolution is increased) to achieve the sharp interface limit. The corresponding solid lines are the results of Cox's theory with different fitting parameters δ . A satisfactory agreement can be found between the simulation results and theoretical results. In addition, according to Kusumaatmaja et al.², a sharp interface limit is approached as $M\mu/\varepsilon^2 \rightarrow \infty$. We keep the mobility M and viscosity μ unchanged and reduce the interface width ε . We plot the functional relationship between $(2R_i/\varepsilon)^2$ and δ in Fig. S2(b). It is found that as $(2R_i/\varepsilon)^2$ increases, the value of δ tends to be convergent, showing a tendency to approach the sharp interface limit. It is noted that in the sharp interface limit, the slip length is proportional to the diffusive length scale $l_S \propto l_D = M\mu/\varepsilon^2$. So the slip length is only dependent on viscosity and mobility. We can thus regulate mobility to achieve different slip lengths in the simulations.

References

1. R. Cox, *Journal of fluid mechanics*, 1986, **168**, 169–194.
2. H. Kusumaatmaja, E. J. Hemingway and S. M. Fielding, *Journal of Fluid Mechanics*, 2016, **788**, 209–227.